ELSEVIER

International Journal of Mass Spectrometry 200 (2000) 443–457

International Journal of Mass Spectrometry

Ion dissociation dynamics and thermochemistry by photoelectron photoion coincidence (PEPICO) spectroscopy

Tomas Baer

Department of Chemistry, University of North Carolina, Chapel Hill, NC 27599-3290, USA

Received 3 July 2000, accepted 30 August 2000

Abstract

Photoelectron photoion coincidence (PEPICO) is a technique that permits the mass spectrometric investigation of energy-selected ions. Dissociation rates and accurate dissociation onsets can be measured. Such data provide not only rigorous tests of the statistical theories for unimolecular reactions, but also provide benchmark heats of formation for anchoring the gas-phase proton affinity scale. When combined with other mass spectrometric methods and quantum calculations of ionic structures, PEPICO provides a means to place the field of ion structures on a firm quantitative basis. Ions are produced by dispersed vacuum ultraviolet radiation in a small electric field in which electrons and ions are extracted in opposite directions. By measuring only ions in coincidence with energy-selected electrons, the ion internal energy is established by conservation of energy [E(ion) = $h\nu$ − IE − $E(el)$]. Recent results as well as new developments in pulsed-field ionization and velocity map imaging are discussed. (Int J Mass Spectrom 200 (2000) 443–457) © 2000 Elsevier Science B.V.

Keywords: Ion dissociation; Thermochemistry; PEPICO

1. Introduction

The production of ions in well-selected energy states is important for the study of ion dissociation rates and the establishment of ion thermochemistry, two endeavors that are closely related. Most ionization methods produce ions in either a broad range of internal energy states (e.g., electron impact), or they produce very-low-energy ions (e.g., electrospray, chemical ionization, field ionization, etc.). In order to produce ions in narrow and selected energy distributions, it is necessary to have an energy-resolved ionization source. Although dispersed vacuum ultraviolet (VUV) radiation is such a source, by itself it does not produce ions in selected energies because the photon energy is distributed between the ion internal energy E_{int} and the kinetic energy of the electron (KE), as shown in Eq. (1).

$$\text{AB} + h\nu \rightarrow \text{AB}^+(E_{\text{int}}) + \text{e}^-(\text{KE}) - \text{IE} \qquad (1)$$

where IE is the molecule's ionization energy. Thus the ion is produced in a range of internal energies, a distribution that can be determined by measuring the photoelectron spectrum at the photon energy, $h\nu$.

The principle of photoelectron photoion coincidence (PEPICO) involves measuring only a subset of ions that are created, namely those that are detected in coincidence with energy-selected electrons [1–3]. In

E-mail: baer@unc.edu

PII S1387-3806(00)00327-4

principle, any electron energy can be chosen, and one approach is to use a fixed energy light source (e.g., the He-discharge lamp at 21.2 eV) and thus chose the ion energy by varying the energy of the electron that is collected [4–6]. This has an economic advantage in that no photon monochromator is required. However, the disadvantage is that the collection efficiency of the electron analyzer is extremely low ($<10^{-3}$) because only a small fraction of the electrons are ejected toward the electron monochromator. This means that of all the ions created at a specific internal energy, E_{int}, less than 1 in 1000 have a chance to be collected in coincidence with their corresponding electron. Thus, the collection efficiency is very low. At the other extreme, is the threshold electron PEPICO approach (TPEPICO) in which the photon energy is varied and the electron energy is fixed at zero energy [7–15]. This has the advantage that initially zero energy electrons can be detected with near unit collection efficiency because they have no initial velocity and thus are extracted by a small electric field in the direction of the detector. In fact, the energy selection in TPEPICO is based mostly on this angular discrimination of energetic electrons. Resolutions of less than 5 meV can be achieved in this manner [16]. The two major disadvantages are the increased complexity of the photon monochromator and the fact that some energetic electrons invariably are initially directed toward the electron detector and thus get collected. The use of a dispersive energy analyzer is only of limited help because the electrons are produced in an electric field of ~10 V/cm. Thus the voltage drop across the ionization region can be several electron volts if the ionization region is 2–3 mm wide. This limits any dispersive analyzer resolution to 2–3 eV. However, if a pulsed source such as a synchrotron is used, it is possible to stop the hot electrons by their time of flight (TOF) [16,17].

An important requirement for PEPICO or TPEPICO is that the light source is continuous in time (or at least of a very high repetition rate) so that the ionization events are distributed in time. Thus, a pulsed laser operating at 10 Hz is not suitable, because many ions and electrons are created with each laser pulse so that the energy-analyzed electron cannot be used to tag the ion with the corresponding energy.

PEPICO experiments have been carried out by a variety of groups for a variety of purposes. The most common experiment has been directed at the unimolecular dissociation of ions. The information derived from PEPICO data are the dissociation rates of energy-selected ions [18–21], the translational energy released in the dissociation [6,22–25], and the breakdown diagram [25–31], which is a plot of the relative ion abundance as a function of the ion internal energy. The dissociation mechanism as well as the thermochemistry for the various fragmentation channels can be extracted from these data. A final application of PEPICO has been the study of ion–molecule reactions with energy-selected reactant ions [32–34]. This latter topic will not be covered here.

The extraction of ion thermochemistry is among the more important applications of photoionization and PEPICO studies. Consider the following dissociative ionization reaction:

$$AB + h\nu \rightarrow A^+ + B + e^- \quad (2)$$

for which an appearance energy (AE) can be experimentally measured. If this AE can be associated with the reaction enthalpy $\Delta H°$, the thermochemistry can be extracted via the energy cycle in Eq. (3):

$$AE \approx \Delta H° = \Delta_f H°(A^+) + \Delta_f H°(B) - \Delta_f H°(AB) \quad (3)$$

Thus, if the heats of formation of any two of the species in reaction (2) are known, the third one can be determined. There are however numerous difficulties in the application of this equation, most of them associated with the relationship between AE and $\Delta H°$.

In many cases, the neutral fragment, B, is small so that its heat of formation and structure are known. However, the structure of the A^+ fragment ion is often not known, nor can it be established on the basis of the photoionization experiment. The results from collisional activation (CA) MS-MS studies offer very attractive additional information to overcome this problem [35–37].

In this article, we review some case studies that

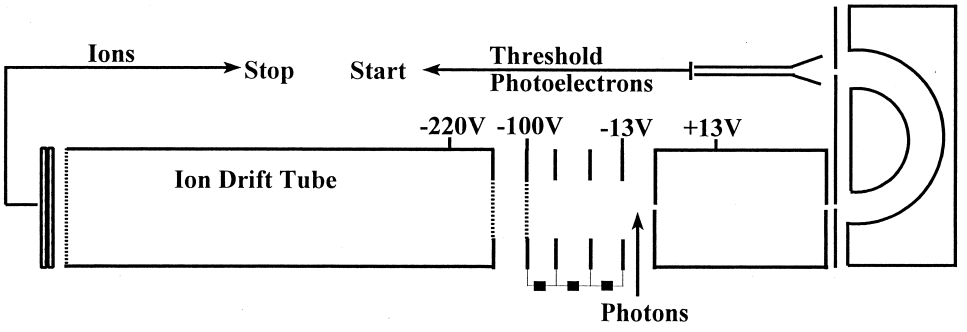

Fig. 1. A typical arrangement of a threshold photoelectron photoion coincidence (TPEPICO) experiment in which the low-energy electrons are preferentially passed by the small holes in the 10-cm-long electron drift tube.

illustrate the procedure for extracting reaction rates, kinetic energy release, and thermochemical information from PEPICO studies. The conclusion will point to some exciting new developments that will enhance the information content of PEPICO studies.

2. Experimental approach

In the standard TPEPICO experiment, tunable vacuum ultraviolet (VUV) radiation is obtained from a continuum source dispersed by a VUV monochromator. This light is used to photoionize molecules in an acceleration region that extracts electrons and ions in opposite directions. A typical arrangement is shown in Fig. 1. Although the electrons pass through a dispersive analyzer, the energy resolution of ~5–20 meV is obtained from the steradiancy analyzer [38–40] that consists of small apertures in the electron drift tube. The small collection angle effectively discriminates against energetic electrons with off-axis velocity components. Thus the energy resolution in threshold photoelectron spectroscopy (PES) is obtained from the angular discrimination rather that the electron energy. In fact, the initially zero-energy electrons that arrive at the detector have an energy spread of 1–3 V depending on the dimensions of the photon beam. A photon beam of 1 mm spread and an acceleration field of 20 V/cm means that electrons are born with a dispersion of 2 eV. As a result, the dispersive analyzer must have a pass energy of 2 eV in order to avoid losing any threshold electrons. Its major function is to stop any scattered electrons that might arise from surface ionization.

In the arrangement shown in Fig. 1, the ions are accelerated through a long first acceleration region, followed by a short second acceleration region, and finally a 30-cm drift region. The electric fields in the two acceleration region are determined by the Wiley–McLaren space focusing conditions [41]. The purpose of the long first acceleration region is to permit measuring ion dissociation rates by modeling the asymmetric TOF distributions. Because one of the major goals of most TPEPICO experiments is the determination of accurate dissociation thresholds, it is essential to measure the dissociation rate constant as a function of energy. This is done so that the derived rate constants, $k(E)$, can be modeled with the RRKM statistical theory [42–44] and extrapolated to the dissociation threshold, E_0. The rate constants for many reactions near threshold are very low ($k < 10^3$) so that ions do not have sufficient time to dissociate in the first acceleration region of Fig. 1. A number of workers thus use a reflectron [45–48] in place of the two-stage linear TOF tube as shown in Fig. 2 [48]. A reflectron consists of two acceleration regions followed by a drift region. The ions then enter a retarding field that reverses their direction. The ions are detected after passing through a second drift region. Metastable ions that dissociate in the first drift region will result in fragment ions that appear at a different TOF than those that were produced in the acceleration regions. If the entry and exit times

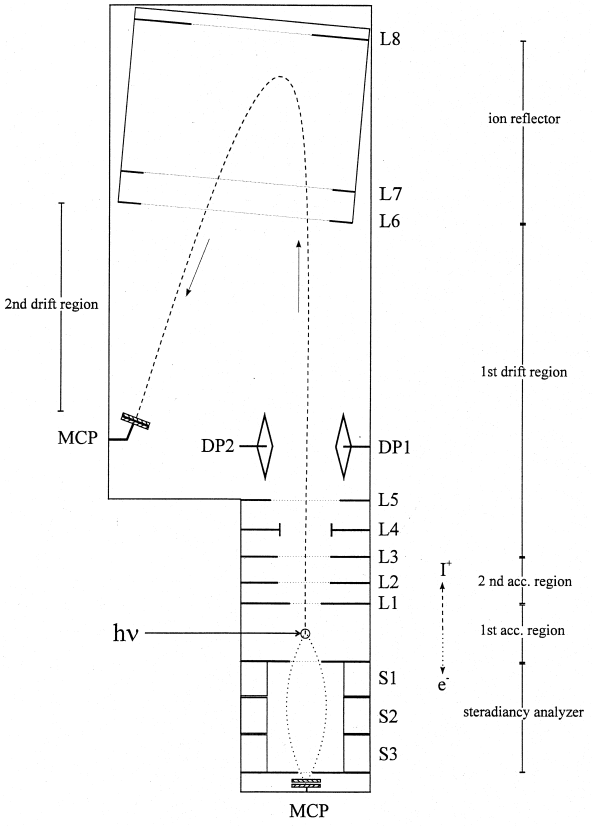

Fig. 2. A typical arrangement of a reflectron TPEPICO set-up. Metastable ions that dissociate in various regions of the ion flight path appear at different final time of flights. Reprinted with permission from Güthe et al. [48].

associated with the first drift region are $\tau 1$ and $\tau 2$, the rate constant can be determined from the ratio of TOF peak areas through the equation:

$$\frac{\text{Area(drift1)}}{\text{Area(total)}} = \frac{\int_{\tau 1}^{\tau 2} e^{-kt}\,dt}{\int_{0}^{\infty} e^{-kt}\,dt} \qquad (4)$$

in which the integrals represent the fragment ion signal obtained between the two limits. The total ion signal in the denominator is the sum of all daughter and parent ion peaks, whereas the numerator is the signal due to dissociation in the first drift region.

3. Examples from the recent literature

3.1. The dissociation of $CpCo(CO)_2$

Cyclopentadienyl cobalt dicarbonyl is a prototype catalyst in which the catalytic site is exposed when the CO group leaves. The catalytic properties thus depend upon the cobalt–carbonyl bond energy and the electronic structure of the exposed metal atom. Fig. 3 shows an energy diagram that summarizes the thermochemical information that can be derived from photoionization data. Of particular interest is the ability to determine the neutral bond energy by measuring the dissociative ionization onset for CO loss and the IE of the neutral CO loss fragment, CpCoCO. The neutral and ion bond energies as well as the heat of formation of the parent molecule can be determined as follows:

$$\text{BE}[\text{CpCoCO}^+\text{–CO}] = \text{AE}[-\text{CO}] - \text{IE}[\text{CpCo(CO)}_2] \quad \text{Ion bond energy} \qquad (5)$$

$$\text{BE}[\text{CpCoCO–CO}] = \text{AE}[-\text{CO}] - \text{IE}[\text{CpCoCO}] \quad \text{neutral bond energy} \qquad (6)$$

$$\Delta_f H°[\text{CpCo(CO)}_2] = \Delta_f H°[\text{Co}^+] + \Delta_f H°[\text{Cp}^{\cdot}] + 2\Delta_f H°[\text{CO}] - \text{AE}[\text{Co}^+ + \text{Cp}^{\cdot} + 2\text{CO}] \qquad (7)$$

Reaction (7) represents a rather novel approach to determining the heat of formation of a neutral molecule. It is possible in organometallic complexes to determine the parent molecule heat of formation from the appearance energy of the complete dissociation because (a) there is no ambiguity in the identification of the neutral species, and (b) the complete dissociation to $Cp^{\cdot} + Co^+ + 2$ CO yields species whose heats of formation are well known. To date, only the loss of the first and second CO group has been measured [49].

Fig. 4 shows TOF data for the CO loss from $CpCo(CO)_2^+$ at two energies close to the dissociation threshold [49]. The very asymmetric fragment ion peak that extends from 28.4 to 30 μs is a result of the slow dissociation in the 5-cm-long acceleration re-

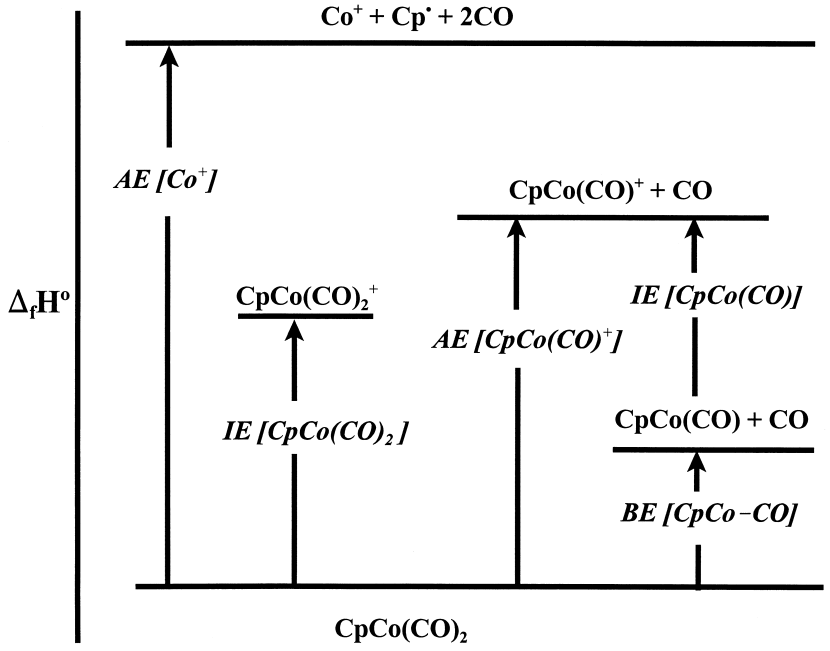

Fig. 3. An energy level diagram for the $CpCo(CO)_2$ complex ($Cp = C_5H_5$). By measuring the quantities indicated by the arrows, it is possible to determine of all the ions as well as the neutral species.

gion. The ×5 expanded TOF distribution shows a step down at ~29.9 μs. This corresponds to the fragment ions that are produced just as the parent ions are exiting the first acceleration region (Fig. 1). All dissociation events in the second acceleration region fall in the TOF range of 29.9 and 30.8 μs. The signal in this region is low because the ions spend little time in this short but strong acceleration region and thus have little time to dissociate. All ions that dissociate in the drift region have nearly the same velocity as their parent ions did, and so will appear approximately at the same time as the parent ions. These are the ions that can be separated from their parent ions in a reflectron mass spectrometer. They could also be separated in a linear arrangement simply by adding an additional acceleration and drift region; but this is rarely done.

The peak widths shown in Fig. 4 result from a combination of the thermal kinetic energy distribution and the kinetic energy release in the dissociation. Because the parent ion does not dissociate, its only source of translational energy is the thermal energy at the temperature of the experiment. This parent TOF width can be dramatically reduced by the use of a molecular beam source that lowers the translational temperature (transverse to the molecular beam) to a few degrees Kelvin [50]. Thus the TOF width can be reduced by a factor of ten.

The solid line is a calculated TOF distribution in which the dissociation rate constant is varied to achieve a good fit. The fixed parameters are the parent and daughter ion masses, and the length and electric fields of the acceleration and drift regions. The calculated TOF distribution is generally convoluted by a Gaussian function to take into account the width of the TOF peaks. The calculated TOF distribution in Fig. 4 also took into account the thermal internal energy distribution of the $CpCo(CO)_2$. Because of the broad thermal distribution, the rate constants, $k(E)$, for the energy-selected ions vary considerably at any one photon energy, so that it is best to average the calculated TOF distribution over this thermal distribution. This method is described in some detail by Sztaray and Baer [49] and Keister et al. [10].

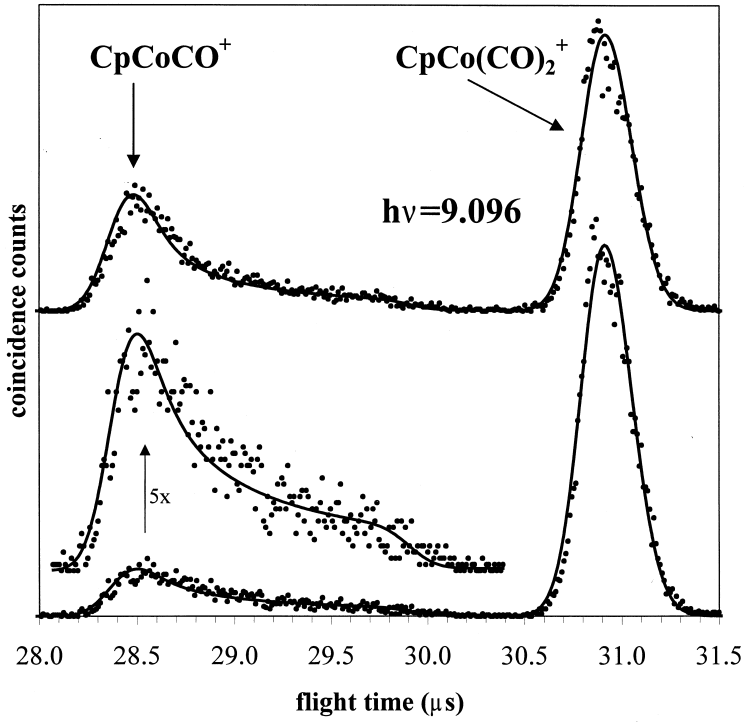

Fig. 4. Time of Flight (TOF) distributions for the products of the energy-selected $CpCo(CO)_2^+$ ion dissociation at the two indicated photon energies. The points are experimental data, while the solid lines are calculated TOF distributions with the dissociation rate constant as an adjustable parameter.

At a photon energy of 9.096 eV, some 100 meV above the first one in Fig. 4, the daughter ion signal has increased relative to the parent ion signal, and the rate constant is higher as evidenced by the more symmetric peak. Similar data were collected at several photon energies. The rate constant function, $k(E)$, that best fits all of the data is shown in Fig. 5. The solid lines through the data points in Fig. 4 are based on this $k(E)$ function. In addition to the first CO loss, the rate constant associated with the second CO loss reaction was also determined and is plotted in Fig. 5. The $k(E)$ functions were generated by RRKM calculations [42–44] using Eq. (8):

$$k(E) = \frac{\sigma N^{\#}(E - E_0)}{h\rho(E)} \tag{8}$$

The density of states, $\rho(E)$, and the sum of states, $N^{\#}(E - E_0)$ were calculated with vibrational frequencies of the parent ion and the transition state determined from ab initio or density functional calculations. The dissociation energy, E_0, was a variable parameter, and the reaction symmetry, σ, was assumed to be 2 for the first CO loss and 1 for the second CO loss. Because the potential energy surface has no real barrier, the transition state was located by variational transition state theory [43,51].

The breakdown diagram, shown in Fig. 6, is the fractional abundance of the parent and daughter ions as a function of the photon energy. The photon energy is related to the parent ion internal energy, E_{int}, by the following equation:

$$E_{\text{int}} = h\nu - \text{IE} + E_{\text{th}} - E_{\text{el}} \tag{9}$$

where $h\nu$ is the photon energy, IE is the adiabatic ionization energy, E_{th} is the parent ion thermal energy, and E_{el} is the electron energy carried away by the electron. Because the latter two quantities are distributions, the parent ion internal energy is given

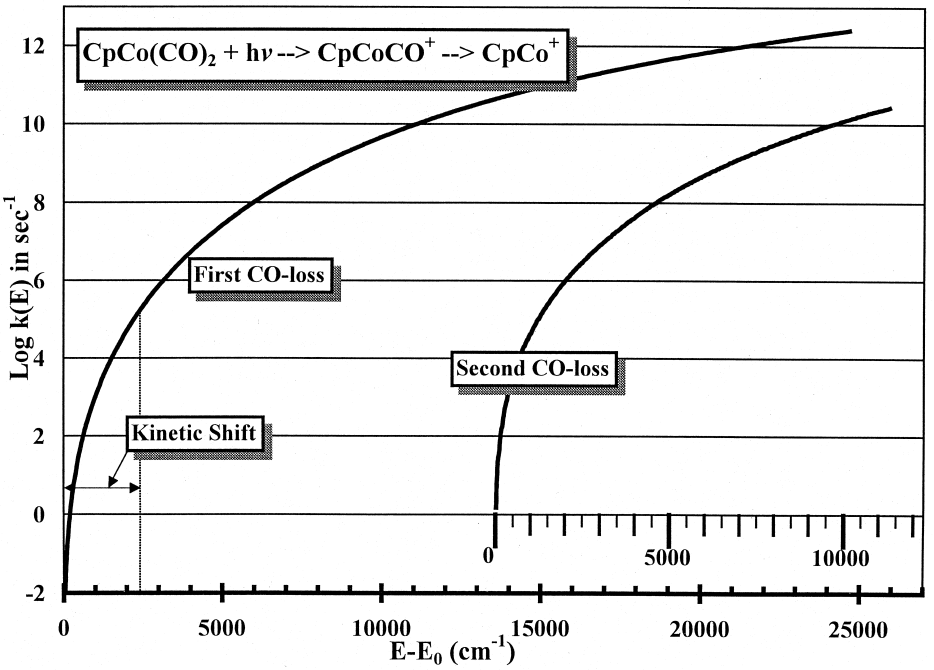

Fig. 5. The derived rate constants for the loss of the first two CO groups as a function of the ion energy above the first dissociation limit. The rate constants are calculated by both RRKM and variational transition state theory. The kinetic shift is indicated.

by a distribution. The E_{th} distribution can be approximated by the thermal energy distribution of the neutral molecule at the temperature of the experiment. In the case of the $CpCo(CO)_2$ molecule, the average thermal energy at room temperature is 120 meV. The E_{el} distribution includes the photon energy resolution (a minor factor at 12 meV) and the asymmetric electron energy analyzer resolution with a width of about 30 meV. The distributions associated with E_{th} and E_{el} have the effect of broadening the breakdown diagram steps. A final factor that needs to be taken into account is the dissociation rate constant. As shown in Fig. 5, the rate constant at the threshold for the first CO loss reaction is 10^{-2} s^{-1}. This means that the mean lifetime of this ion would be 100 s. Vibrationally excited ions cannot live this long without stabilizing by infrared fluorescence [52,53]. In addition, long lived ions do not dissociate sufficiently fast for the ion to fragment in the first acceleration region ($\sim$6.5 μs) and thus are detected as parent, rather than daughter ions. In fact, the fragment ion will not be seen until the rate constant reaches $\sim 10^5$ s^{-1}. Thus, as shown in Fig. 5, the onset energy appears shifted to higher energies (kinetic shift) [54–56]. For the case of the $CpCo(CO)_2^+$ ion dissociation, this kinetic shift is $\sim$0.3 eV. On the other hand, the thermal energy distribution of the parent ion shifts the onset to lower energies. When all of these effects are taken into account, the calculated 0K thermochemical dissociation limit is located at the energy given by the dashed line in Fig. 6. In a similar fashion, the dissociation limit for the second CO loss reaction is also determined.

3.2. H_2 elimination via tunneling in ethane ions

It is evident in Fig. 4 that rate constants measured by fitting the TOF distribution in the first acceleration region can only be measured if the mass of the fragment ion is considerably smaller than that of the parent ion. For instance, H and H_2 loss fragments have a TOF that is so close to that of the parent ion that the asymmetry in the TOF distribution cannot be

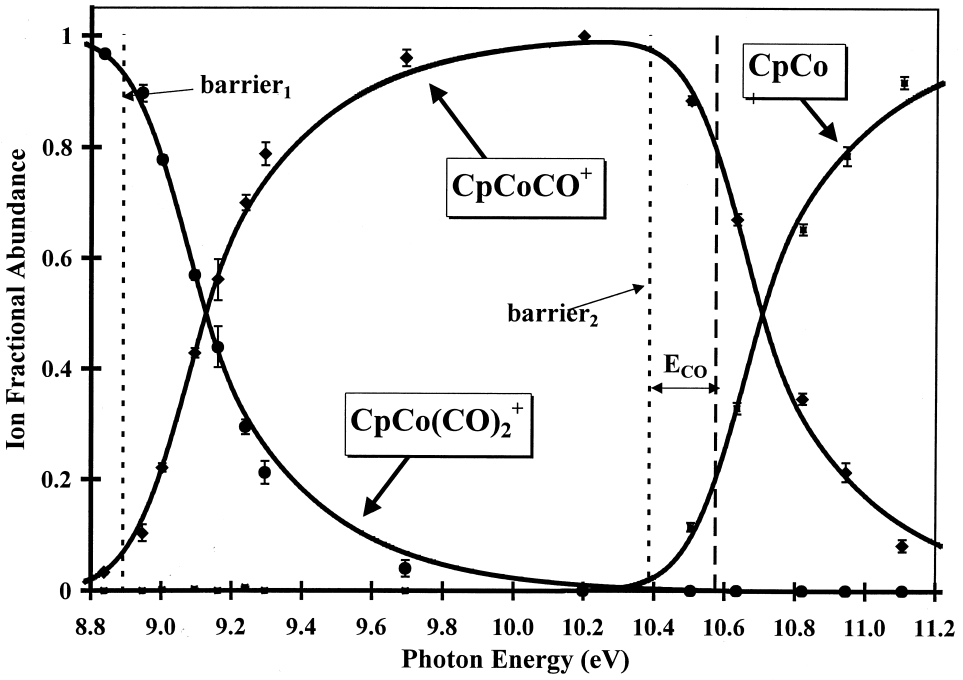

Fig. 6. The $CpCo(CO)_2$ breakdown diagram (ion abundance vs ion photon energy) showing the loss of the first two CO groups. The dashed lines are the 0K dissociation limits (barriers 1 and 2) which have been determined by convoluting the 0K breakdown diagram with the thermal energy distribution. The larger dashed line shows the average energy carried away by the first CO group. Reprinted with permission from Sztaray and Baer [49].

analyzed with much precision. The H_2 loss rate constant from the ethane ion would thus be very difficult to extract by this method. On the other hand, the use of a reflectron TOF (RETOF) in Fig. 2, permits the investigation of such reactions. Fig. 7 shows the TOF distributions obtained when ethane is ionized at several photon energies from 12.018 to 12.200 eV [46]. At low energies, the parent ion at 24.0 μs dominates whereas by 12.20 eV, the parent ion is completely dissociated. The identity of the various daughter ion peaks is best shown in Fig. 8 in which the peaks are labeled by their mass. The $C_2H_3^+$ peak labeled as 29, is a result of light from the higher order (24.16 eV) synchrotron radiation light. The other three peaks are due to the H_2 loss fragment, $C_2H_4^+$. The peak labeled 28_{acc} corresponds to daughter ions formed in the first acceleration region. Evident is a slight asymmetry, the origin of which is the same as the daughter ion peak in Fig. 4, but now much reduced because the first acceleration region (Fig. 2) used by Güthe et al. [48] is much shorter. The peak labeled as 28_{drift} is a result of dissociation in the drift region (see Fig. 2). It appears at a longer TOF because it traveled as a heavy parent ion through the first acceleration region prior to dissociation in the drift region. The final very small and broad peak labeled 28_{ref} is a result of ions that dissociate in the reflectron region. It is broad because the TOF depends on where in the reflectron the dissociation took place.

As mentioned previously, the rate constants for dissociation can be determined from the ratios of the various peaks (see for instance, Eq. 4). The four peaks provide three unique ratios that can be checked for internal consistency. When these data are analyzed by including the thermal energy content of the ethane molecule (mostly rotational energy), the rate constants shown in Fig. 9 are obtained. This figure shows that rate constants ranging from 10^3 to 10^6 s^{-1} can be determined with a reflectron. The use of the linear TOF instrument (Fig. 1) extends the rate to about 5×10^6 s^{-1}.

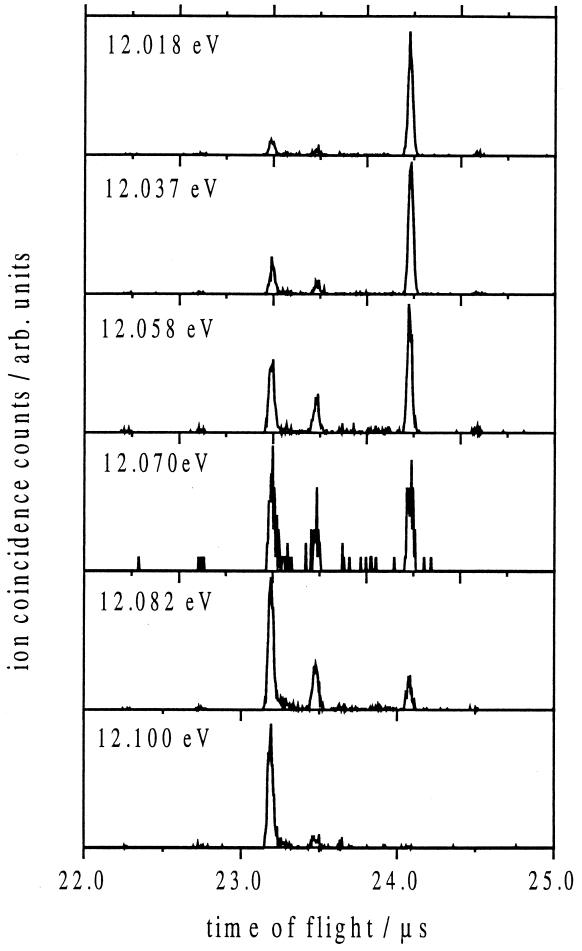

Fig. 7. The TOF distributions of $C_2H_4^+$ (23.3 − 23.8 μs), and parent $C_2H_6^+$ (24 μs) ions at several photon energies from the TPEPICO experiment with a reflectron. Reprinted with permission from Güthe and Weitzel [46].

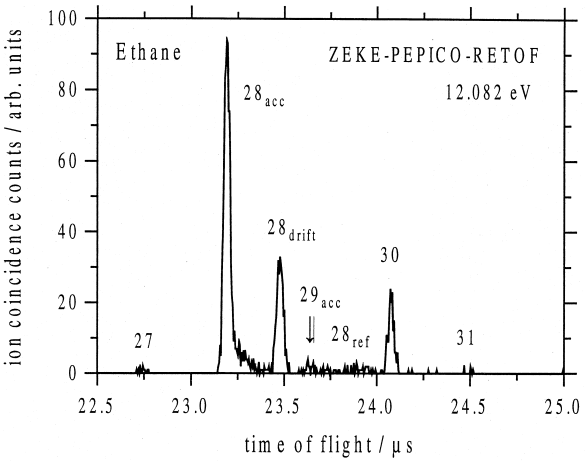

Fig. 8. Detail of the TOF distribution at 12.082 eV. The main peak labeled 28_{acc} is ascribed to dissociation in the first acceleration region, whereas the peak labeled 28_{drift} is assigned to ethene ions produced in the first drift region (see Fig. 2). 28_{ref} is due to ions that have dissociated in the reflectron. Reprinted with permission from Güthe and Weitzel [46].

An interesting aspect of the $k(E)$ curve in Fig. 9 is the rapid rise in the rate constant, which increases by more than three orders of magnitude in less than 100 meV. This rapid rise, and the fact that the ethane ion is metastable at all, strongly suggests that the reaction proceeds via tunneling. A small ion such as ethane has few vibrational frequencies and thus a small density of states. In addition, the apparent activation energy for H_2 loss as measured by the difference in the AE and IE is only 0.55 eV, which again suggests a low density of states for the molecular ion in the vicinity of the dissociation limit [46]. According to the RRKM theory (Eq. 8), if $\rho(E)$ is small, the rate constant should be fast. For these reasons, Weitzel and coworkers analyzed their results by assuming that the rate determining step is tunneling through an H atom transfer barrier [57,58]. The RRKM equation, modified to include tunneling is given by Eq. (10)

$$k(E) = \frac{\sigma \int_0^{E-\Delta E} \rho^{\#}(E-\varepsilon)\kappa(\varepsilon)\, d\varepsilon}{h\rho(E)} \quad (9)$$

in which κ is the tunneling probability, ΔE is the reaction endoergicity, and ϵ is the energy in the reaction coordinate. In this expression, the energies are referenced to the zero point energy of the molecular ion. A computationally simpler approach is to reference the energy at the top of the classical barrier [43,59].

Tunneling rates can be readily calculated by using the one-dimensional Eckart potential [60] for which closed forms for the tunneling probability are available [43,59]. The input for these calculations are the barrier height, the endoergicity, and the curvature at the top of the barrier. This curvature is obtained directly from the imaginary vibrational frequency that

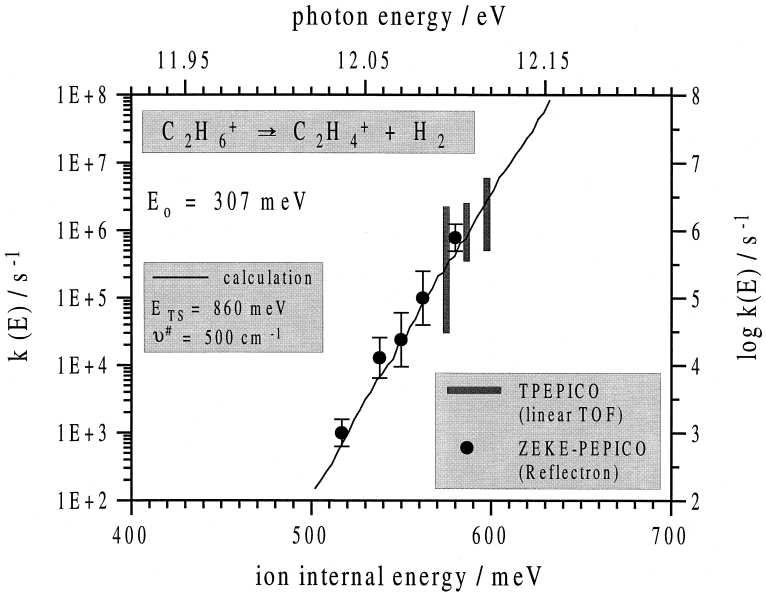

Fig. 9. The derived rate constant for the H_2 loss reaction from ethane ions. The points are experimental rate constants, while the line through the points are based on an RRKM calculation that includes the tunneling through an Eckart barrier. Reprinted with permission from Güthe and Weitzel [46].

is calculated for a transition state. The transition state resides on a point in the potential energy surface, where motion away from equilibrium for all normal modes leads to an increase in the energy, except for the normal mode associated with the reaction coordinate. The latter resides at a maximum. A three-dimensional analog is like a pass in the mountains in which the hiking path over the pass is the reaction coordinate, and the mountains on either side represent the vibrational potential of the second normal mode. Thus $v - 1$ of the vibrational frequencies at the transition state are real, while the frequency associated with the reaction coordinate is imaginary (it appears as a negative frequency in the ab initio calculation). Weitzel and co-workers calculated the potential energy surface for the H_2 loss from the ethane ion and found it to have a barrier height of 1.006 eV and an endoergicity of 0.307 eV. As is evident from Fig. 9, barrier penetration already begins at an energy of 0.510 eV, and by 0.6 eV the rate constant is well out of the metastable range.

In the case of the ethane ion dissociation, the slow dissociation rate constant and its rapid rise provide clues about the dissociation mechanism. In particular, the data as well as ab initio calculations [57] confirm that the rate-determining step involves an H atom transfer step. Because the rates are metastable only over a small energy interval, data without energy selection would not have provided sufficient information to permit drawing these conclusions.

In the case of reactions that proceed via tunneling, the potential energy surface can be quite simple. All that is required is that the rate-limiting step involve an H atom transfer. Many reactions of organic ions are complicated because they proceed via several isomerization steps, some of which may involve tunneling. Recent studies have shown that some organic ions dissociate by two-component decay rates [61–64]. These ions dissociate either rapidly and directly from their initial structure, or they isomerize to lower energy species, from which they dissociate more slowly. The isomerized ions dissociate more slowly because the ion internal energy is larger so that the density of states is correspondingly larger, resulting in a larger denominator in Eq. (8). Whether ions dissociate via tunneling or via isomerization, the net result

is that the rate constants are lower than expected. It is not entirely trivial to determine for which reason the dissociation is slow. Ab initio calculations of the potential energy surface and H/D isotopic substitution are required to establish the cause.

4. Recent advances and prospects for the future

4.1. Pulsed field ionization PEPICO study of methane and acetylene

One of the major problems with the TPEPICO technique is that energetic electrons initially ejected in the direction of the electron analyzer are detected unless they can be discriminated against by their TOF. However, the latter approach requires the use of a pulsed photon source. A number of synchrotron sources operate in the few-bunch mode, in which the time between photon pulses is between 100 and 1000 ns, sufficiently long to permit electron TOF analysis and thus to improve the electron resolution to ~5 meV. Even better resolution can be obtained by the use of pulsed field ionization (PFI) or ZEKE. This technique, developed by Müller-Dethlefs and Schlag [65,66] normally uses laser excitation of very high n Rydberg states. These electronic states, which are just a few wave numbers below the ionization continuum, can be stabilized by stray fields [67–69]. By waiting for a microsecond, during which time the free electrons are lost, it is possible to pulse field ionize the high Rydberg states, because as neutrals they remain in the ionization region. The mechanism for stabilization of the high Rydberg states (they are stable for up to 10 μs) is not fully understood, but it is felt that the inhomogeneous fields generated by the ions during the laser pulse play a key role in converting the initial low ℓ states into high ℓ and m_ℓ quantum states through Stark mixing.

Weitzel and Güthe [70] first showed that PFI/ZEKE experiments are also possible with quasicontinuous synchrotron radiation in which the continuous production and extraction of ions ensures that no ions will be present when a high Rydberg state is created. The key advantage of the synchrotron in using PFI to generate electrons and ions, is that it is possible to also measure the ion in coincidence with the field-ionized electron, a feature that is absent in pulsed laser experiments in which many ions and electrons are generated during the 10-ns laser pulse.

The trend in modern synchrotron sources is toward multibunch operation, in which the time between photon pulses is so small (~1 ns) that timing of electrons is no longer possible. However, following the suggestion of Waterstradt et al. [71], Jarvis et al. [72] developed an approach that uses the dark gap in the synchrotron bunches to distinguish the prompt from the field-ionized electrons with excellent suppression of hot electrons. When combined with ion detection, it made possible the use of continuous synchrotron radiation for PFI-PEPICO experiments in which a resolution of 1 meV was achieved [73–75]. A key requirement for PFI experiments is the use of a very high-resolution photon monochromator so that the narrow band of Rydberg states just below the ionization energy can be excited. Details about the experimental aspects and a discussion of PFI spectra can be found in an accompanying paper by C.Y. Ng in this volume.

A breakdown diagram for the acetylene ion is shown in Fig. 10 [73]. Although the electron energy resolution is 1 meV, the rotational and vibrational internal energy distribution at room temperature of most molecules is much broader than this. Thus, the breakdown diagram does not show as sharp a transition from the parent to the daughter ion as might be expected. However, the 0K dissociation limit at 17.3576 ± 0.0010 eV shown by the arrow is clearly evident as the energy at which the parent ion signal disappears. The two breakdown diagrams differ in that the circles include the internally cold and hot acetylene ions, whereas the squares include only the cold part. The two samples were distinguished by the width of their TOF peaks. The two methods of analysis yield the identical 0K dissociation limit.

Neutral acetylene is one of the few molecules with an exceptionally well-established bond energy of 5.7125 ± 0.0010 eV. When this is combined with the dissociative ionization limit determined in this study, the ionization potential of the $C_2H^{\cdot}$ can be calculated

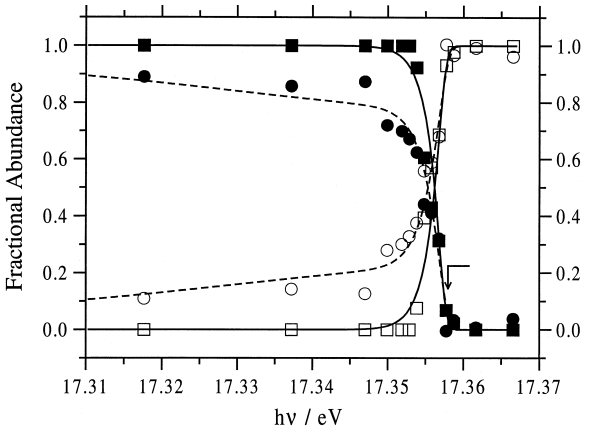

Fig. 10. The breakdown diagram for H loss from the acetylene ion obtained by a pulsed field ionization-PEPICO experiment with sub-milli eV resolution. The open data include warm acetylene sample, whereas the solid data include only the acetylene molecules that have been cooled in the supersonic expansion. The two signals were distinguished by their peak widths. The lines through the points are calculated breakdown diagrams that take into account the thermal energy distribution of the acetylene molecules. The arrow shows the 0K dissociation onset. Reprinted with permission from Jarvis et al. [73].

to be 11.6451 ± 0.0010 eV. This IE has yet to be measured to 10 meV accuracy. Additionally, it is apparent that the limiting factor in determining the $C_2H^{\cdot}$ free radical heat of formation is the heat of formation of the acetylene molecule. A similar study of the CH_4^+ ion dissociation yielded a dissociative photoionization onset for H atom loss of 14.323 ± 0.001 eV [75]. Other PFI-PEPICO studies have been carried out on C_3H_7X (X=Cl, Br, I) [76]; and C_2H_5I [77]. In the case of the C_3H_7X study, a new value for the $\Delta_fH°(C_3H_7^+)$ was derived, which leads to a new proton affinity of 742.3 ± 1/5 kJ/mol (at 298K). This value is nearly 10 kJ/mol lower than the Hunter and Lias recommended value [78].

4.2. Electron-ion imaging experiments: $NO^+ \rightarrow N^+ + O$

Another exciting new technique for PEPICO studies involves ion and electron imaging in which position sensitive detectors are used for either the electrons, or ions, or both particles. A very interesting version of this is velocity map imaging [79–83]. The first reported study of velocity map imaging pointed out that instead of using grids to separate regions of electric fields from drift regions, as is normally done in ion and electron TOF optics, there are substantial advantages that accrue from the elimination of grids and the use of focusing optics [81]. The basic idea, which is easily verified by ion trajectory calculations using SIMION [84], is that an extended or large ion source of equal velocity electrons or ions (perpendicular to the particle flight path) can be focused to an annular ring with a width of less than 100 μm. This spacial focusing is not possible with the use of grids so that a source width of 5 mm will always limit the spacial resolution of the charged particles at the position sensitive detector. With velocity map imaging, an extended source is equivalent to a point source when grids are used.

In the ultimate version of imaging experiments, timing and position sensitive detectors are used for both electrons and ions [80,83,85]. An example of such a set-up is shown in Fig. 11 with which Lafosse et al. [85] have recently investigated the dissociation dynamics of NO^+ ions in the vicinity of 23.75 eV. Because of the open structure of the electron and ion optics, electrons and ions of all energies (up to ~4 eV) can be collected. The TOF provides information about the initial velocity in the direction of the detector. When combined with the position information, the angle and total initial kinetic energy can be derived. Thus all angle- and energy-resolved electrons can be correlated with their corresponding angle- and energy-resolved product ions (in this case N^+). The total information content is very large, and ways must be found to present parts of it in meaningful ways. Fig. 12 shows a two-dimensional contour plot of the signal intensity versus the electron and N^+ kinetic energy. The largest peak labeled I, is associated with the ejection of energetic electrons of 2 eV and the production of low-energy (0.35 eV) N^+ ions. By conservation of momentum, the total translational energy associated with the ion and the O atom must be 0.66 eV. The electron energy of 2 eV associated with a photon energy of 23.75 eV means that the NO^+ ions were produced with an internal energy of 21.75 eV (*c*

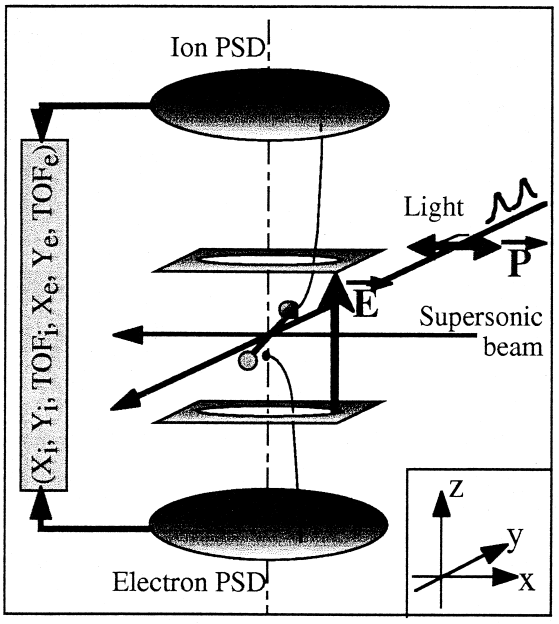

Fig. 11. The experimental arrangement of the imaging experiment in which the TOF and position of both electrons and ions were determined. Various angular correlations between the electron and the ion fragment can be derived from the multidimensional data. Reprinted with permission from Lafosse et al. [85].

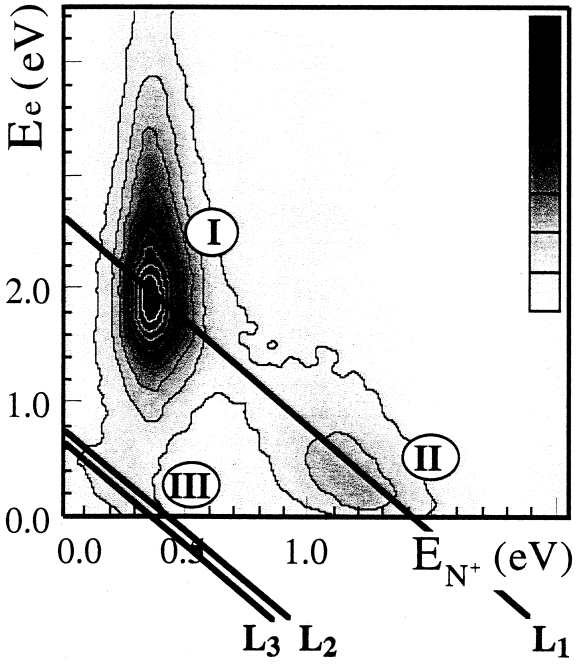

Fig. 12. A two-dimensional contour plot of the electron and ion coincidence intensity versus the electron and ion kinetic energies for the dissociative photoionization of NO to $N^+ + O$ in which the products can be formed in a variety of electronic states. The dominant channels, indicated as I and II lead to the production of $N^+(^3P) + O(^3P)$, but from different NO^+ electronic states. A minor channel (III) leads to low translational energy, but high electronic energy products. Reprinted with permission from Lafosse et al. [85].

$^3\Pi$ state). By subtracting the total translational energy of 0.66 eV from this *c* state energy, we can deduce that the products are $N^+(^3P)$ and $O(^3P)$ at an energy of 21.1 eV. The next most important peak, labeled II is associated with low-energy electrons, but high-energy ions. When the electron energy of 0.4 eV is added to the N^+ energy of 1.2 eV and the corresponding O atom energy of 1.05 eV, energy conservation indicates that the same $N^+(^3P) + O(^3P)$ limit at 21.1 eV is reached. This is also evident by the line labeled L_1 in Figure 12. The other process, labeled III is associated with a small electron energy and a small ion kinetic energy and shows that the final state produced is either the $N^+(^1D) + O(^3P)$ limit at 22.90 eV or the $N^+(^3P) + O(^1D)$ limit at 22.92 eV. These two limits are shown as the lines L_2 and L_3.

This example is just a small fraction of the complete information that is contained in the data. It highlights the kinetic energy release information that can be derived. Of special note is the fact that quantitative branching ratios to the final product states are obtained because all electrons and ions are detected with equal probability, regardless of their translational energies or their initial angle of ejection. In addition to the kinetic energy release and the branching ratios, the data contain a wealth of angular distribution information including all the vector correlations between the departing electron and the N^+ ion. Because the products are atomic species, all of the energy is fully accounted for. When this type of experiment is applied to polyatomic ions, the information will be less detailed. However, the ability to collect coincidence signal of ions with electrons of various energies, rather than just threshold electrons will be very valuable, because the state of the ion produced may well depend on the manner in which the ions are produced. This was noted some time ago

in the case of the CF_3I^+ dissociation dynamics, in which it was found that nominally identical energy ions decayed differently when produced with threshold electrons and with energetic electrons [86].

5. Conclusions

Photoelectron photoion coincidence spectroscopy is an extremely versatile tool for investigating the dissociation dynamics of ions as well as ion molecule reactions. High-resolution studies, especially with angle-resolved methods on small ions can lead to very detailed understanding of the ionic behavior at the quantum level. The application of PEPICO to the study of larger ions has been revolutionized by the ability to calculate ionic structures and vibrational frequencies by ab initio and density functional methods. By careful consideration of the molecule's thermal energy and the dissociation rate as a function of the ion internal energy, accurate dissociation limits can be extracted. These values are essential for establishing quantitative heats of formation for ions, and they also provide one of the most effective means for determining neutral bond energies.

Acknowledgements

The author is grateful to the Department of Energy for support of the work in his laboratory. Thanks also to my collaborators, K.M. Weitzel, Marcus Malow, Balint Sztaray, Yue Li, C.Y. Ng, Gary Jarvis, and Yang Song.

References

[1] B. Brehm, E.V. Puttkamer, Z. Naturforsch. A22 (1967) 8.
[2] J.H.D. Eland, Int. J. Mass Spectrom. Ion. Processes 9 (1972) 397.
[3] T. Baer, in M.T. Bowers (Ed.), Gas Phase Ion Chemistry, 1st ed. Academic Press, New York, 1979, Ch. 5.
[4] J. Dannacher, Chem. Phys. 29 (1978) 339.
[5] J.H.D. Eland, Int. J. Mass Spectrom. Ion. Processes 12 (1973) 389.
[6] I. Powis, Chem. Phys. 74 (1983) 421.
[7] Q. Zha, T. Nishimura, G.G. Meisels, Int. J. Mass Spectrom. Ion. Processes 83 (1988) 1.
[8] D.M. Smith, R.P. Tuckett, K.R. Yoxall, K. Codling, P.A. Hatherly, Chem. Phys. Lett. 216 (1993) 493.
[9] O. Dutuit, T. Baer, C. Metayer, J. Lemaire, Int. J. Mass Spectrom. Ion. Processes 110 (1991) 67.
[10] J.W. Keister, T. Baer, R. Thissen, C. Alcaraz, O. Dutuit, H. Audier, V. Troude, J. Phys. Chem. A 102 (1998) 1090.
[11] H.M. Rosenstock, R. Stockbauer, A.C. Parr, J. Chim. Phys. 77 (1980) 745.
[12] W. Kamke, J.D. Vries, J. Krauss, E. Kaiser, B. Kamke, V. Hertel, Z. Phys. D. Atoms, Molecules, Clusters 14 (1989) 339.
[13] Y. Morioka, M. Ogawa, T. Matsumoto, K. Ito, K. Tanaka, T. Hayaishi, J. Phys. B: Atom. Molec. Phys. 24 (1991) 791.
[14] K. Norwood, C.Y. Ng, J. Chem. Phys. 91 (1989) 2898.
[15] K.M. Weitzel, J. Mahnert, M. Penno, Chem. Phys. Lett. 224 (1994) 371.
[16] F. Merkt, P.M. Guyon, J.W. Hepburn, Chem. Phys. 173 (1993) 479.
[17] P.M. Guyon, T. Baer, L.F.A. Ferreira, I. Nenner, A. Tabche-Fouhaile, R. Botter, T.R. Govers, J. Phys. B: Atom. Molec. Phys. 11 (1978) L141.
[18] J. Dannacher, H.M. Rosenstock, R. Buff, A.C. Parr, R. Stockbauer, R. Bombach, J.P. Stadelmann, Chem. Phys. 75 (1983) 23.
[19] H.M. Rosenstock, R. Stockbauer, A.C. Parr, J. Chem. Phys. 71 (1979) 3708.
[20] R. Bombach, J. Dannacher, J.P. Stadelmann, J. Am. Chem. Soc. 105 (1983) 4205.
[21] T. Baer, Adv. Chem. Phys. 64 (1986) 111.
[22] T. Baer, U. Buchler, C.E. Klots, J. Chim. Phys. 77 (1980) 739.
[23] B.E. Miller, T. Baer, Chem. Phys. 85 (1984) 39.
[24] K. Johnson, I. Powis, C.J. Danby, Chem. Phys. 70 (1982) 329.
[25] R. Stockbauer, Int. J. Mass Spectrom. Ion. Processes 25 (1977) 401.
[26] A.C. Parr, A.J. Jason, R. Stockbauer, Int. J. Mass Spectrom. Ion. Processes 26 (1978) 23.
[27] A.C. Parr, A.J. Jason, R. Stockbauer, K.E. McCulloh, Int. J. Mass Spectrom. Ion. Processes 30 (1979) 319.
[28] A.C. Parr, A.J. Jason, R. Stockbauer, Int. J. Mass Spectrom. Ion. Processes 33 (1980) 243.
[29] T. Baer, O. Dutuit, H. Mestdagh, C. Rolando, J. Phys. Chem. 92 (1988) 5674.
[30] P.R. Das, T. Nishimura, G.G. Meisels, J. Phys. Chem. 89 (1985) 2808.
[31] K. Norwood, A. Ali, G.D. Flesch, C.Y. Ng, J. Am. Chem. Soc. 112 (1990) 7502.
[32] T.R. Govers, P.M. Guyon, T. Baer, K. Cole, H. Frohlich, M. Lavollee, Chem. Phys. 87 (1984) 373.
[33] P.M. Guyon, T. Baer, S.K. Cole, T.R. Govers, Chem. Phys. 119 (1988) 145.
[34] C.Y. Ng, in J.M. Farrar, W.H. Saunders Jr. (Eds.), Techniques for the Study of Ion-Molecule Reactions, John Wiley, New York, 1988, Ch. 8.
[35] N. Heinrich, T. Drewello, P.C. Burgers, J.C. Morrow, J. Schmidt, W. Kulik, J.K. Terlouw, H. Schwarz, J. Am. Chem. Soc. 114 (1992) 3776.

[36] R. Feng, C. Wesdemiotis, M.Y. Zhang, M. Marchetti, F.W. McLafferty, J. Am. Chem. Soc. 111 (1989) 1986.
[37] T. Nishishita, F.W. McLafferty, Org. Mass Spectrom. 12 (1977) 75.
[38] T. Baer, W.B. Peatman, E.W. Schlag, Chem. Phys. Lett. 4 (1969) 243.
[39] T. Hsieh, J. Gilman, M. Weiss, G.G. Meisels, P.M. Hierl, Int. J. Mass Spectrom. Ion. Proc. 36 (1980) 317.
[40] R. Spohr, P.M. Guyon, W.A. Chupka, J. Berkowitz, Rev. Sci. Instrum. 42 (1971) 1872.
[41] W.C. Wiley, I.H. McLaren, Rev. Sci. Instrum. 26 (1955) 1150.
[42] T. Baer, P.M. Mayer, J. Am. Soc. Mass Spectrom. 8 (1997) 103.
[43] T. Baer, W.L. Hase, Unimolecular Reaction Dynamics: Theory and Experiments, Oxford University Press, New York, 1996.
[44] T. Baer, in T. Baer, C.Y. Ng, I. Powis, (Eds.), The Structure, Energetics, and Dynamics of Organic Ions, John Wiley, Chichester, 1996, Ch. 3.
[45] U. Boesl, R. Weinkauf, E.W. Schlag, Int. J. Mass Spectrom. Ion. Processes 112 (1992) 121.
[46] F. Güthe, K.M. Weitzel, Ber. Bunsenges. Phys. Chem. 101 (1997) 484.
[47] H. Krause, H.J. Neusser, J. Chem. Phys. 97 (1992) 5923.
[48] F. Güthe, M. Malow, K.M. Weitzel, H. Baumgärtel, Int. J. Mass Spectrom. Ion. Processes 172 (1998) 47.
[49] B. Sztaray, T. Baer, J. Am. Chem. Soc. 122 (2000) 9219.
[50] J.S. Riley, T. Baer, Int. J. Mass Spectrom. Ion. Processes 131 (1994) 295.
[51] W.L. Hase, Chem. Phys. Lett. 139 (1987) 389.
[52] R.C. Dunbar, J.H. Chen, H.Y. So, B. Asamoto, J. Chem. Phys. 86 (1987) 2081.
[53] R.C. Dunbar, Mass Spectrom. Rev. 11 (1992) 309.
[54] W.A. Chupka, J. Chem. Phys. 30 (1959) 191.
[55] F.S. Huang, R.C. Dunbar, J. Am. Chem. Soc. 112 (1990) 8167.
[56] C. Lifshitz, Mass Spectrom. Rev. 1 (1982) 309.
[57] K.M. Weitzel, Int. J. Mass Spectrom. Ion. Processes 136 (1994) 1.
[58] K.M. Weitzel, J. Mähnert, Z. Phys. Chem. 195 (1996) 181.
[59] W.H. Miller, J. Am. Chem. Soc. 101 (1979) 6810.
[60] C. Eckart, Phys. Rev. 35 (1930) 1303.
[61] L.M. Duffy, J.W. Keister, T. Baer, J. Phys. Chem. 99 (1995) 17862.
[62] O.A. Mazyar, T. Baer, Int. J. Mass Spectrom. Ion. Processes 185 (1999) 165.
[63] O.A. Mazyar, P.M. Mayer, T. Baer, Int. J. Mass Spectrom. Ion. Processes 167/168 (1997) 389.
[64] O.A. Mazyar, T. Baer, J. Phys. Chem. A 102 (1998) 1682.
[65] O. Dopfer, G. Reiser, K. Muller-Dethlefs, E.W. Schlag, S.D. Colson, J. Chem. Phys. 101 (1994) 974.
[66] K. Muller-Dethlefs, E.W. Schlag, Ann. Rev. Phys. Chem. 42 (1991) 109.
[67] W.A. Chupka, J. Chem. Phys. 98 (1993) 4520.
[68] F. Merkt, J. Chem. Phys. 100 (1994) 2623.
[69] F. Merkt, H.H. Fielding, T.P. Softley, Chem. Phys. Lett. 202 (1993) 153.
[70] K.M. Weitzel, F. Güthe, Chem. Phys. Lett. 251 (1996) 295.
[71] E. Waterstradt, R. Jung, H.J. Dietrich, K. Muller-Dethlefs, Rev. Sci. Instrum. 64 (1993) 3104.
[72] G.K. Jarvis, Y. Song, C.Y. Ng, Rev. Sci. Instrum. 70 (1999) 2615.
[73] G.K. Jarvis, K.M. Weitzel, M. Malow, T. Baer, Y. Song, C.Y. Ng, Phys. Chem. Chem. Phys. 1 (1999) 5259.
[74] G.K. Jarvis, K.M. Weitzel, M. Malow, T. Baer, Y. Song, C.Y. Ng, Rev. Sci. Instrum. 70 (1999) 3892.
[75] K.M. Weitzel, M. Malow, G.K. Jarvis, T. Baer, Y. Song, C.Y. Ng, J. Chem. Phys. 111 (1999) 8267.
[76] T. Baer, Y. Song, C.Y. Ng, J. Liu, W. Chen, J. Phys. Chem. A 104 (2000) 1559.
[77] T. Baer, Y. Song, J. Liu, W. Chen, C.Y. Ng, Faraday Discuss. 115 (2000) 137.
[78] E.P.L. Hunter, S.G. Lias, J. Phys. Chem. Ref. Data 27 (1998) 413.
[79] D.W. Chandler, D.H. Parker, Adv. Photochem. 25 (1999) 59.
[80] J.A. Davies, J.E. LeClaire, R.E. Continetti, C.C. Hayden, J. Chem. Phys. 111 (1999) 1.
[81] D.H. Parker, A.T.J.B. Eppink, J. Chem. Phys. 107 (1997) 2357.
[82] J.C. Pinare, B. Baguenard, C. Bordas, M. Broyer, Phys. Rev. Lett. 81 (1998) 2225.
[83] M. Takahashi, J.P. Cave, J.H.D. Eland, Rev. Sci. Instrum. 71 (2000) 1337.
[84] D.A. Dall. SIMION 3D. [Version 6]. 43ed ASMS Conference on Mass Spectrometry and Allied Topics, May 21–26 1995, Atlanta, GA, p. 717 (sis@sisweb.com).
[85] A. Lafosse, M. Lebech, J.C. Brenot, P.M. Guyon, O. Jagutzki, L. Spielberger, M. Vervloet, J.C. Houver, D. Dowek, Phys. Rev. Lett. 84 (2000) 5987.
[86] I. Powis, Chem. Phys. Lett. 189 (1992) 473.